

# Magic angle twisted bilayer graphene as a highly efficient quantum Otto engine

Ayush Singh\* and Colin Benjamin†

School of Physical Sciences, National Institute of Science Education and Research, HBNI, Jatni 752050, India

At a discrete set of *magic angles*, twisted bilayer graphene has been shown to host extraordinarily flat bands, correlated insulating states, unconventional superconductivity, and distinct Landau level degeneracies. In this work, we design a highly efficient quantum Otto engine using a twisted bilayer graphene sample. Flat electronic bands at magic angles make the prospect of extracting work from our Otto engine lucrative because exploiting correlated phenomena may lead to nanoscale devices are operating at more considerable efficiencies. We use an eight-band continuum model of twisted bilayer graphene to compute efficiencies and work outputs for magic and non-magic angle twists and compare the results with an *AB* stacked bilayer and a monolayer. It is observed that the efficiency varies smoothly with the twist angle, and the maximum is attained at the magic angle.

## I. INTRODUCTION

One of the ways to approach quantum thermodynamics [1] is to design and study thermodynamic cycles designed as quantum analogs of classical thermodynamic processes. These cycles use quantum matter as a “working substance” to convert thermal energy to valuable work. In the literature, quantum analogs of adiabatic, isochoric, isothermal [2] and isobaric [3] process have been described, and some general results with quantum thermodynamic cycles, like Carnot and Otto, have been derived [2–7].

Due to the quantum nature of the working substance, quantum heat engines (QHEs) are expected to exhibit some unique properties that allow better performance than their classical counterparts. For example, it has been shown that quantum heat engines can extract work from a single heat bath [8], and under certain conditions even surpass the Carnot limit [9, 10]. Hence, QHEs can be used to convert thermal energy to practical work in nanoscale devices efficiently. In addition to this, studying quantum thermodynamic cycles allows us to test the robustness of thermodynamic principles in a quantum setting. Moreover, since the language used to describe QHEs is quite general, the same discussion can be applied to phenomena ranging from lasers and photosynthetic light harvesting [10–13] to information theory and quantum computation [14–16].

Quantum thermodynamic processes are carried out either by quasistatically changing the temperature of the heat reservoir—which the working substance is kept in equilibrium with—or by varying some tunable parameter that changes the energy spectrum of the quantum system. In magnetically driven quantum heat engines, Landau levels are changed by varying an external magnetic field [17–20]. It is convenient because it is generally easier to quasistatically modulate the external field than some internal parameter of the working substance [17]. Magnetically driven quantum heat engines based on a semiconductor quantum dot [17, 18] and monolayer graphene flake [19, 21] have been proposed, however, these are by no means the only kinds of QHEs possible.

In this paper, we propose a magnetically driven quantum heat engine based on twisted bilayer graphene. Interest in

twisted bilayer graphene (TBG) and other Moiré materials have exploded in the last few years because of band topology, electronic and optical properties of Moiré systems can be tuned by engineering the relative twist between layers. In particular, at a discrete set of magic angles, TBG hosts exceptionally flat electronic bands where Fermi velocity vanishes and the two layers get strongly coupled [22, 23]. Flat bands are interesting because they can lead to highly correlated phenomena such as superconductivity [24], insulating states at half-filling [25], isospin Pomeranchuk effect [26] and an electronic phase transition at zero magnetic field [27]. A quantum heat engine based on twisted bilayer graphene is, therefore, a great avenue to study the interplay of electronic properties of Moiré systems with quantum thermodynamics, statistical physics, and quantum information.

In this paper, we present calculations for a quantum analog of the Otto cycle [2, 5, 28] based on bilayer graphene, and observe that the efficiency increases when the layers are twisted with respect to each other and approaches the maximum at the magic angle. For computing Landau levels in TBG, we use an eight-band approximation of the non-interacting continuum model Hamiltonian [22, 23, 29, 30] which reproduces the Fermi velocity with reasonable accuracy down to the first magic angle [22], and diagonalize it numerically [31].

The rest of this paper is organized as follows: we start by reviewing Landau levels in magic-angle twisted graphene (MATBG), followed by a description of the Otto engine cycle. Expressions for work output and efficiency are derived, and the results are compared for monolayer, bilayer, and magic-angle twisted bilayer.

## II. LANDAU LEVELS IN MONOLAYER AND BILAYER GRAPHENE

Since our proposed quantum heat engine uses a graphene flake under transverse magnetic field as working substance, we present here a brief review of Landau levels in monolayer and bilayer graphene. The treatment here closely follows [32] for monolayer and [33] for bilayer graphene.

Effective low energy Hamiltonian for monolayer graphene near valley points is

$$h_m(\mathbf{k}) = \xi \hbar v_F \boldsymbol{\sigma} \cdot \mathbf{k}, \quad (1)$$

\* ayush.singh@niser.ac.in

† colin.nano@gmail.com

where  $\xi = \pm$  is the *valley pseudospin*,  $v_F \sim 10^6 \text{ m s}^{-1}$  is Fermi velocity,  $\sigma = (\sigma_x, \sigma_y)$  are Pauli matrices, and  $\mathbf{k} = (k_x, k_y)$  is crystal momentum. This Hamiltonian leads to massless Dirac fermions with Berry phase  $\pi$  [32]. In order to incorporate magnetic field we use the gauge transformation  $\mathbf{p} \rightarrow \boldsymbol{\pi} = \mathbf{p} + e\mathbf{A}$ , where  $\mathbf{A}$  is magnetic vector potential and charge of electron is  $-e$ . For a transverse magnetic field  $\mathbf{B} = (0, 0, B)$ , vector potential in Landau gauge becomes  $\mathbf{A} = (0, Bx, 0)$  which results in  $\pi_x = p_x$  and  $\pi_y = p_y + eBx$ . With canonical commutation relations  $[x_i, p_j] = i\hbar\delta_{ij}$ , it can be shown that the operators,

$$\Pi = \frac{1}{\sqrt{2e\hbar B}}(\pi_x - i\pi_y) \quad \text{and} \quad \Pi^\dagger = \frac{1}{\sqrt{2e\hbar B}}(\pi_x + i\pi_y), \quad (2)$$

satisfy the algebra of harmonic oscillator ladder operators i.e.,  $[\Pi, \Pi^\dagger] = 1$ . In terms of these ladder operators the Hamiltonian (1) can be written as,

$$h_m = \xi\sqrt{2}\frac{\hbar v_F}{l_B} \begin{bmatrix} 0 & \Pi \\ \Pi^\dagger & 0 \end{bmatrix}, \quad (3)$$

where we have introduced *Landau radius*  $l_B = \sqrt{\hbar/eB}$ . Eigenvalue equation for (3) can be solved exactly to give Landau levels for monolayer graphene [32],

$$E_n = \pm \frac{\hbar v_F}{l_B} \sqrt{2n}, \quad n = 1, 2, 3, \dots \quad (4)$$

where  $\pm$  is the *band index* labelling conduction and valence bands, and  $n$  is Landau level index. We neglect Zeeman splitting and note that each  $n$ -state is fourfold degenerate due to spin and valley degeneracies. For  $n = 0$ , we get a fourfold degenerate ground state at zero energy.

In tight-binding model for  $AB$  stacked bilayer graphene, there are four nearest-neighbour tunnelling processes: intralayer hopping, dimer hopping and two non-dimer hoppings, and we get massive Dirac fermions with Berry phase  $2\pi$  [33, 34]. If we only consider intralayer and dimer hoppings in tight-binding model, a low energy Hamiltonian can be derived,

$$h_b(\mathbf{k}) = -\frac{1}{2m_{\text{eff}}} \begin{bmatrix} 0 & \Pi^2 \\ (\Pi^\dagger)^2 & 0 \end{bmatrix}, \quad (5)$$

which admits an analytical solution for Landau levels,

$$E_n = \pm \hbar\omega_B \sqrt{n(n-1)}, \quad n = 2, 3, 4, \dots \quad (6)$$

where  $\omega_B = eB/m_{\text{eff}}$  is *cyclotron frequency* with effective mass  $m_{\text{eff}} \approx 0.035m_e$  [33, 34]. Like in case of monolayer, each  $n$  state is fourfold degenerate due to spin and valley degeneracies, but both  $n = 0$  and  $n = 1$  are zero energy states and ground state is therefore eightfold degenerate. This spectrum is valid only for small level index and low magnetic fields because, in obtaining (5), the trigonal warping term due to  $\gamma_3$  was dropped, and orbitals relating to dimer sites due to  $\gamma_4$ , were eliminated [33]. In particular, we require  $n\hbar\omega_B \ll 3 \text{ eV}$ , which is easy to satisfy for a heat engine operating around 100 K in which only first few Landau levels are occupied.

## A. Model for twisted bilayer graphene

The low energy continuum model Hamiltonian for twisted bilayer graphene consists of three parts: two single layer Hamiltonians for intralayer hopping and a term for tunnelling between layers [22, 23, 29]. The single layer Hamiltonian, rotated by an angle  $\theta$  for an isolated graphene sheet near Dirac point is

$$h_\theta(\mathbf{k}) = \mathcal{D}(\hat{z}, \theta) [-\hbar v_F \boldsymbol{\sigma} \cdot \mathbf{k}] \mathcal{D}^{-1}(\hat{z}, \theta), \quad (7)$$

where  $\mathbf{k} = (k_x, k_y)$  is crystal momentum,  $\boldsymbol{\sigma} = (\sigma_x, \sigma_y)$  are Pauli matrices and  $\mathcal{D}(\hat{z}, \theta) = e^{-i\sigma_z\theta/2}$  is the rotation matrix. Dirac points of the two rotated graphene layers are separated by  $k_\theta = (8\pi/3a) \sin(\theta/2)$ , where  $a = 2.46 \text{ \AA}$  is the lattice constant [22]. For interlayer tunnelling, an analysis of Moiré patterns shows that, for small twist angles there are three main tunnelling processes, with hopping directions (cf. Fig. 1)

$$\mathbf{q}_b = k_\theta(0, -1), \quad \mathbf{q}_{\text{tr}} = k_\theta \left( \frac{\sqrt{3}}{2}, \frac{1}{2} \right), \quad \mathbf{q}_{\text{tl}} = k_\theta \left( \frac{-\sqrt{3}}{2}, \frac{1}{2} \right),$$

which are characterized by matrices,

$$T_b = \begin{bmatrix} 1 & 1 \\ 1 & 1 \end{bmatrix}, \quad T_{\text{tr}} = \begin{bmatrix} e^{-i\phi} & 1 \\ e^{i\phi} & e^{-i\phi} \end{bmatrix}, \quad T_{\text{tl}} = \begin{bmatrix} e^{i\phi} & 1 \\ e^{-i\phi} & e^{i\phi} \end{bmatrix} \quad (8)$$

where  $\phi = 2\pi/3$  [22, 30, 35]. Repeated hopping generates a honeycomb lattice in the momentum space. Truncating the continuum model Hamiltonian [22, 23, 29] at the first honeycomb shell, gives rise to the following eight-band Hamiltonian:

$$\mathcal{H}_\theta = \begin{bmatrix} h_{\theta/2}(\mathbf{k}) & wT_b & wT_{\text{tr}} & wT_{\text{tl}} \\ wT_b^\dagger & h_{-\theta/2}(\mathbf{k}_b) & 0 & 0 \\ wT_{\text{tr}}^\dagger & 0 & h_{-\theta/2}(\mathbf{k}_{\text{tr}}) & 0 \\ wT_{\text{tl}}^\dagger & 0 & 0 & h_{-\theta/2}(\mathbf{k}_{\text{tl}}) \end{bmatrix}, \quad (9)$$

where  $\mathbf{k}_j = \mathbf{k} + \mathbf{q}_j$  and  $w \approx 110 \text{ meV}$  is the interlayer hopping energy [22, 31]. The Hamiltonian  $\mathcal{H}_\theta$  acts on a four-dimensional vector of two-component spinors, which is why it is called an eight-band model [31].

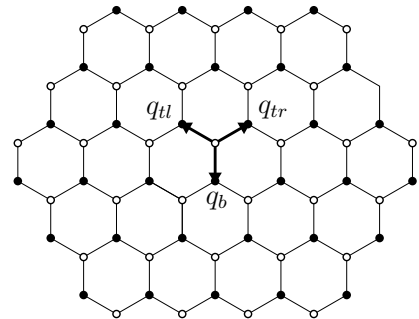


FIG. 1. Momentum space lattice of twisted bilayer graphene. Three equivalent Dirac points result in three distinct tunnelling processes. For all three processes  $|\mathbf{q}_j| = k_\theta$  and the hopping directions are:  $(0, -1)$  for  $\mathbf{q}_b$ ,  $(\sqrt{3}/2, 1/2)$  for  $\mathbf{q}_{\text{tr}}$  and  $(-\sqrt{3}/2, 1/2)$  for  $\mathbf{q}_{\text{tl}}$ .

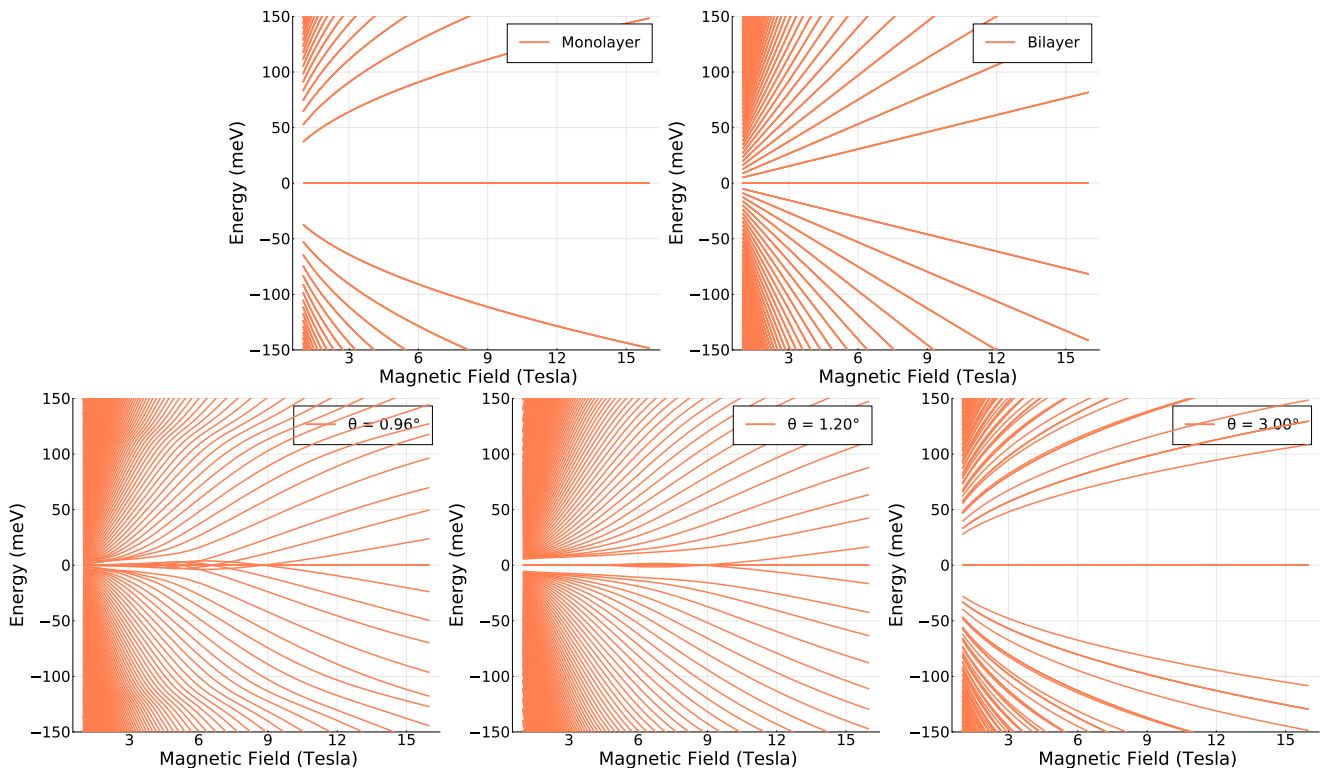


FIG. 2. Landau level spectra for twisted bilayer graphene. The most important feature of these plots is the dispersion of energy levels concerning the magnetic field. For monolayer Landau levels go as  $E_n \sim \sqrt{B}$ , for bilayer the dispersion is linear  $E_n \sim B$ . With a small twist, Landau levels around zero energy start having a flat dispersion, and as the twist is increased the Landau level spectrum starts looking remarkably similar to the monolayer. The peculiar nature of magic-angle induced flat bands near zero energy for  $\theta^* = 0.96^\circ$  should be noted.

The angle dependence of  $h_\theta$  is parametrically small and can be neglected, and it was shown in [22] that the eight-band approximation reproduces correct Fermi velocity with reasonable accuracy to the first magic angle. Up to a scale factor, the electronic structure of the eight-band model depends on dimensionless parameter  $\alpha = w/\hbar v_F k_\theta$ , in terms of which we can write renormalized Fermi velocity [22],

$$\frac{v'_F}{v_F} = \frac{1 - 3\alpha^2}{1 + 6\alpha^2}, \quad (10)$$

which vanishes at  $\theta^* \approx 0.96^\circ$ . It is where the magic angle occurs in the model. Moreover, it is the only magic angle the eight-band model can reproduce since we are truncating the momentum space lattice at the first honeycomb shell. Refs [30, 36, 37] describe, in detail, the procedure for obtaining Landau levels in TBG, with full continuum model Hamiltonian. We also note that several qualitative features of TBG like flat bands and interpolation of electronic the structure between bilayer and monolayer behavior can also be seen in ab-initio tight-binding calculations of the band structure [38].

### B. Numerically computing Landau levels in twisted bilayer graphene

As the ladder operators introduced in the previous section obey  $[\Pi, \Pi^\dagger] = 1$ , we have harmonic oscillator states

$|0\rangle, |1\rangle, |2\rangle, \dots$  satisfying  $\Pi^\dagger \Pi |n\rangle = n |n\rangle$ . These states constitute a complete, orthonormal basis set for this Hilbert space.  $\Pi^\dagger$  and  $\Pi$  act as raising and lowering operators for these states with  $\Pi^\dagger |n\rangle = \sqrt{n+1} |n+1\rangle$  and  $\Pi |n\rangle = \sqrt{n} |n-1\rangle$  respectively. Using these relations, it can be verified that the matrix representation of ladder operators in this basis is

$$\langle n | \Pi | m \rangle = \sqrt{m} \delta_{n, m-1} \quad \text{and} \quad \langle n | \Pi^\dagger | m \rangle = \sqrt{m+1} \delta_{n, m+1}. \quad (11)$$

To find Landau level spectrum, the substitution  $\hbar k \rightarrow \pi$  is made in an eight-band Hamiltonian, and it is written in terms of these ladder operators. However, as the harmonic oscillator states do not constitute an eigenbasis of the Hamiltonian, this representation is not diagonal, and the energy eigenvalues have to be determined numerically. [39].

In principle, the basis  $\{|n\rangle\}_{n=0,1,2,\dots}$ , is infinite, but for practical purposes, we truncate it after a large, but finite number of states:  $|0\rangle, |1\rangle, \dots, |N\rangle$ . For all calculations, we have retained  $N = 500$  harmonic oscillator states for finding Landau levels. In our trials, it was observed that retaining fewer Landau levels resulted in deviations in energy eigenvalues at low magnetic fields, while retaining more than 500 Landau levels resulted in considerable execution times without any significant improvement in accuracy.

Landau level spectra obtained by numerically diagonalizing the Hamiltonian have been plotted in Fig. 2. The most striking feature of these plots are the dispersion of energies to the

magnetic field. In TBG, especially at magic angles, the peculiar nature of flat bands near zero energy should be noted. At larger twist angles, as the two layers get decoupled, qualitative features of the TBG spectrum and the dispersion for the magnetic field are very similar to monolayer, except for a renormalized Fermi velocity [22, 31]. The efficiency of the Otto cycle depends, almost exclusively, on the dispersion of Landau levels for the magnetic field. It is discussed in detail in the sections dealing with quantum heat engine cycles and results and discussion.

### III. QUANTUM HEAT ENGINE CYCLE

For the heat engine, we shall consider an ensemble of single electron states in the conduction band [17–19, 21]. We take Landau levels  $|\psi_n\rangle$  with energies  $E_n$  and occupation probabilities  $p_n$ , so that the density matrix is  $\rho = \sum_n p_n |\psi_n(B)\rangle\langle\psi_n(B)|$ . Average energy of this ensemble,  $U = \text{Tr}(\rho\mathcal{H}_\theta) = \sum_n p_n E_n$  is identified as *internal energy* of the system, and we can state a quantum version of the first law of thermodynamics [2, 5, 14],

$$dU = dQ + dW = \sum_n E_n dp_n + \sum_n p_n dE_n. \quad (12)$$

Since thermodynamic entropy  $S = -k_B \sum_n p_n \ln p_n$ , and in classical thermodynamics, heat exchanged  $dQ = TdS$ , we identify  $dQ = \sum_n E_n dp_n$  and work as  $dW = \sum_n p_n dE_n$  [2, 5, 14]. From density matrix, we can calculate von Neumann entropy,

$$S(T, B) = -k_B \text{Tr}(\rho \ln \rho) = -k_B \sum_n p_n \ln p_n. \quad (13)$$

Occupation probabilities of different energy levels are determined by the temperature of working substance [2, 17]. The temperature of the working substance is controlled either by keeping it in equilibrium with a heat bath and varying its temperature quasistatically, or by coupling it to hot and cold reservoirs alternatively [7, 9, 28]. At temperature  $T$ , occupation probabilities satisfy The Boltzmann distribution, which is given as,

$$p_n(T, B) = \frac{e^{-\beta E_n(B)}}{Z(T, B)}; \quad Z(T, B) = \sum_{n=0}^{\infty} e^{-\beta E_n(B)}, \quad (14)$$

with  $\beta = 1/k_B T$  and  $Z(T, B)$  being partition function. In what follows, we shall assume that the thermal reservoir is a classical object and that its temperature can be varied quasistatically. We shall also assume that external magnetic field can be varied quasistatically to modulate Landau levels  $E_n$ , and their occupation probabilities  $p_n$ .

Quantum Otto cycle consists of four strokes, operating between magnetic field strengths  $B_1$  and  $B_2$  (with  $B_2 > B_1$ ), and temperatures  $T_C$  and  $T_H$  (with  $T_H > T_C$ ). In order to draw parallels with classical Otto cycle, it is easier to state the compression and expansion strokes in terms of decreasing and increasing *Landau radius*  $l_B = \sqrt{\hbar/eB}$ .

Before discussing details of the cycle, we take a moment to note the differences between the general and strict versions of the adiabatic stroke. In the general version of the

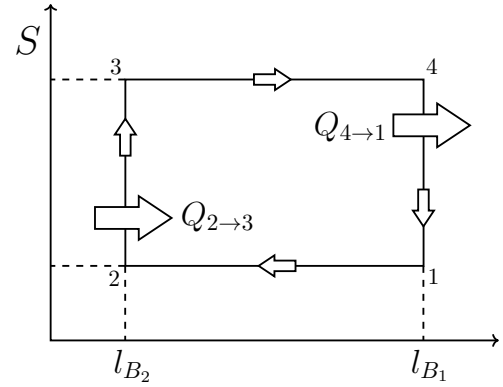


FIG. 3. Four strokes of Otto cycle on an entropy–magnetic field plot. The cycle starts with an adiabatic compression  $1 \rightarrow 2$ , in which Landau radius decreases due to an increase in magnetic field, followed by an isochoric absorption of heat  $2 \rightarrow 3$ . Next, magnetic field is decreased adiabatically  $3 \rightarrow 4$  and finally heat is rejected isochorically  $4 \rightarrow 1$  to return the system to its initial state.

adiabatic stroke, the working substance is kept in thermal equilibrium, and the temperature of the heat reservoir is changed gradually. The entropy remains constant throughout the process. In particular, in an adiabatic process when temperatures and magnetic fields change  $(T_i, B_i) \rightarrow (T_f, B_f)$ , we require  $S(T_i, B_i) = S(T_f, B_f)$ . In the strict version of the adiabatic process, we impose a stronger constraint and require the occupation probabilities of energy states to remain unchanged  $p_n(i) = p_n(f)$  [2, 20]. In particular, at the end of the stricter version of the adiabatic stroke, the system need not be in a state with well-defined temperature [2]. The "stricter" and "general" versions of the adiabatic stroke might look very different and lead to different work output and efficiency. However, both these conditions can be shown to be equivalent when the energy levels change in the same ratio (cf. Appendix B). In what follows, we focus on a heat engine cycle with general adiabatic stroke and leave the details of the cycle with strict adiabatic strokes to appendix B.

The first stroke is an adiabatic compression in which Landau radius is reduced by gradually increasing the external magnetic field. Due to this changing magnetic field, we have  $l_{B_1} \rightarrow l_{B_2}$ . However, since entropy has to be held constant, temperature must also change  $T_C \rightarrow T_2$ , to satisfy adiabatic condition  $\Delta S = 0$  and the intermediate temperature  $T_2$  is determined by the condition

$$S(T_C, B_1) = S(T_2, B_2). \quad (15)$$

In the second stroke, the working substance absorbs heat from the reservoir, while Landau radius is held constant at  $l_{B_2}$  and acquires a temperature  $T_H$  at the end of the process. This is called a *hot isochore* [9, 28]. Heat absorbed in this stroke

can be calculated from (12),

$$\begin{aligned} Q_{2 \rightarrow 3} &= \int_2^3 \sum_{n=0}^{\infty} E_n(B_2) dp_n \\ &= \sum_{n=0}^{\infty} E_n(B_2) [p_n(T_H, B_2) - p_n(T_2, B_2)] \end{aligned} \quad (16)$$

The next stroke is an adiabatic expansion and involves an increase of Landau radius  $l_{B_2} \rightarrow l_{B_1}$ . As the temperature changes  $T_H \rightarrow T_4$  the general adiabatic condition reads:

$$S(T_H, B_2) = S(T_4, B_1). \quad (17)$$

In the final stroke, heat is lost to reservoir, with Landau radius being held constant at  $l_{B_1}$  as the system attains the temperature  $T_C$  and the cycle can be started over again. This process is called a *cold isochore* [9, 28]. Heat exchanged in this stroke can be calculated as before,

$$Q_{4 \rightarrow 1} = \sum_{n=0}^{\infty} E_n(B_1) [p_n(T_C, B_1) - p_n(T_4, B_1)]. \quad (18)$$

Since no heat exchange occurs in adiabatic processes, and working substance returns to its initial state at end of cycle, we can use quantum first law with  $\Delta U = 0$  to write work output of engine as

$$|W_O| = Q_{\text{cycle}} = |Q_{2 \rightarrow 3}| - |Q_{4 \rightarrow 1}|, \quad (19)$$

while efficiency is given by,

$$\eta_O = \frac{|W_O|}{|Q_{\text{in}}|} = \frac{|Q_{2 \rightarrow 3}| - |Q_{4 \rightarrow 1}|}{|Q_{2 \rightarrow 3}|} = 1 - \frac{|Q_{4 \rightarrow 1}|}{|Q_{2 \rightarrow 3}|} \quad (20)$$

$$= 1 - \frac{\sum_n E_n(B_1) [p_n(T_C, B_1) - p_n(T_4, B_1)]}{\sum_n E_n(B_2) [p_n(T_H, B_2) - p_n(T_2, B_2)]}, \quad (21)$$

where in the last line, we used (16) and (18).

The discussion up to this point has been entirely general since all these results are direct consequences of the quantum first law of thermodynamics. Eqs. (19) and (21) are equally applicable to any quantum working substance coupled to a classical thermal reservoir. Very similar expressions for work and efficiency appear, for example, in [2, 5, 17, 18, 21].

#### IV. RESULTS AND DISCUSSION

In case of *AB* stacked bilayer graphene, where an analytical expression for Landau levels is known i.e.

$$E_n = \hbar \omega_B \sqrt{n(n-1)}, \quad n = 0, 1, 2, \dots \quad (22)$$

with  $\omega_B = eB/m_{\text{eff}}$  [33, 34], we note that the energy levels change in the same ratio and constraints on  $T_2$  and  $T_4$  are equivalent to the strict adiabatic conditions (cf. Appendix B)

$$p_n(T_C, B_1) = p_n(T_2, B_2) \text{ and } p_n(T_H, B_2) = p_n(T_4, B_1). \quad (23)$$

We can use (21) to derive the Otto efficiency,

$$\eta_O^{\text{bi}} = 1 - \left| \frac{\omega_{B_1}}{\omega_{B_2}} \right| = 1 - \left( \frac{l_{B_2}}{l_{B_1}} \right)^2 = 1 - r_C^{-2}, \quad (24)$$

where we have defined the *compression ratio*  $r_C = l_{B_1}/l_{B_2}$  so that the efficiency is reminiscent of the classical expression  $\eta_O = 1 - r_C^{-(\gamma-1)}$  [40]. Similarly, for monolayer graphene, we have [32]

$$E_n = \frac{\hbar v_F}{l_B} \sqrt{2n}, \quad n = 0, 1, 2, \dots \quad (25)$$

and therefore,

$$\eta_O^m = 1 - \left| \frac{l_{B_2}}{l_{B_1}} \right| = 1 - r_C^{-1}. \quad (26)$$

As already stated, in both monolayer and bilayer graphene, general and stricter versions are equivalent.

For twisted bilayer graphene, a simple expression for Landau level energies is not known, and therefore an analytic expression for efficiency cannot be derived. In the classical cycle temperatures  $T_2$  and  $T_4$  have to be determined numerically from adiabatic conditions (15) and (17), and efficiency has to be computed directly from (21). Efficiencies and work outputs are plotted for different angles in Fig. 4 and Fig. 5 respectively. For all numerical computations,  $N = 500$  Landau levels were retained.

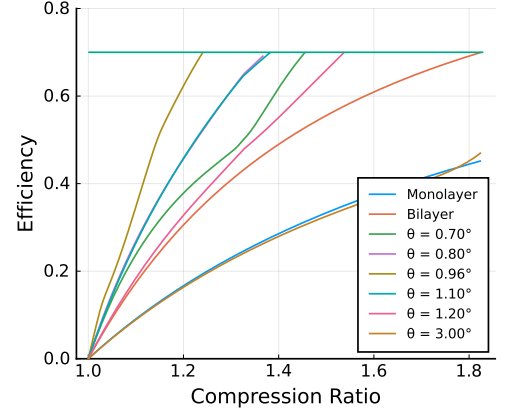


FIG. 4. Efficiencies as a function of the compression ratio for Otto cycles operating between  $T_C = 30$  K and  $T_H = 100$  K, and  $B_1 = 5.0$  T. Different twist angles are plotted together for comparison.

Some partial insight into increased efficiencies can be ascertained by looking at qualitative differences in Landau level plots for monolayer, bilayer, and magic angle twisted bilayer graphene. If the Landau levels have the dispersion  $E_n(B) = l_B^{-\alpha} f(n) = (eB/\hbar)^{\alpha/2} f(n)$  then, from (21) we have

$$\eta_O = 1 - r_C^{-\alpha}. \quad (27)$$

Furthermore, efficiencies obtained by direct numerical computation can be fitted for the parameter  $\alpha$  in (27) and a larger value of  $\alpha$  in dispersion of  $E_n$  is responsible for higher efficiency.

It is what we see in Landau level plots for twisted bilayer. After attaining a maximum at  $\theta^* = 0.96^\circ$  (magic angle) the efficiency starts falling for larger twist angles until it coincides with monolayer efficiency for  $\theta = 3.0^\circ$ . It is to be expected because, for larger twists, the two layers get decoupled.

The take-home message of our paper is the following: proposed quantum Otto engine has the highest efficiency at magic angle  $\theta^* = 0.96^\circ$ .

Work output is obtained by directly computing the difference between heat absorbed (16) and heat lost (18) during the cycle. Work is plotted as a function of compression ratio in Fig. 5. For each case, work output initially increases as the compression ratio is increased, and after attaining a maximum, starts falling and eventually reaches zero just as efficiency reaches Carnot limit  $\eta_C = 1 - T_C/T_H$ . Zero work output at Carnot efficiency can be interpreted as a manifestation of the second law of thermodynamics in these systems. In particular, we note that the proposed heat engine cannot surpass the Carnot limit despite operating with a quantum working substance as the cycle is composed of equilibrium processes committed to operating between two temperatures [7, 17, 41].

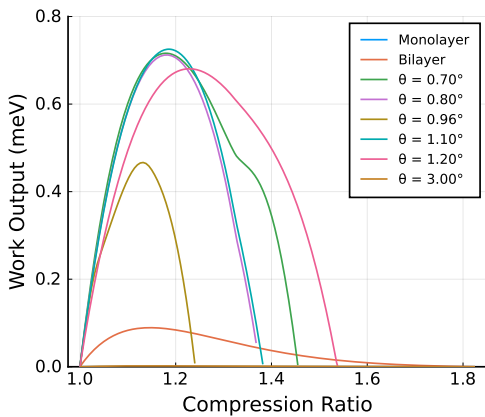


FIG. 5. Work output as a function of compression ratio at different twist angles, for cycles operating between  $T_C = 30$  K and  $T_H = 100$  K, and magnitude  $B_1 = 5.0$  T. Different twist angles are plotted together for comparison.

Finally, we note that a dip in work output at the magic angle. Due to flat bands, Landau levels which are predominantly occupied during the cycle (according to Eq. 14), have energy very close to zero. Therefore heat absorbed (16) and rejected (18) during the cycle are significantly smaller, resulting in lower work output.

## V. EXPERIMENTAL REALIZATION AND CONCLUSION

Until this point, we have not referred to any specific properties of the heat reservoir to which the working substance couples during the hot and cold isochores. In experimental realizations of quantum Otto cycles, the details of the heat reservoir depend strongly on the working substance. For example, in a single-ion heat engine, [28] the hot and cold reservoirs are realized by detuned lasers at different frequencies, while in a spin quantum

TABLE I. A comparison of efficiencies and work outputs for Otto cycle.

Working Substance	Efficiency	Work (meV)
Monolayer Graphene	$1 - r_C^{-1.00}$	0.000169
Semiconductor	$1 - r_C^{-1.98}$	1.143
Bilayer Graphene	$1 - r_C^{-2.00}$	0.0758
$\theta = 0.70^\circ$	$1 - r_C^{-2.68}$	0.669
$\theta = 0.80^\circ$	$1 - r_C^{-3.48}$	0.650
Twisted Bilayer Graphene $\theta^* = 0.96^\circ$	$1 - r_C^{-5.03}$	0.438
$\theta = 1.10^\circ$	$1 - r_C^{-3.47}$	0.671
$\theta = 1.20^\circ$	$1 - r_C^{-2.37}$	0.608
$\theta = 3.00^\circ$	$1 - r_C^{-0.98}$	0.00159

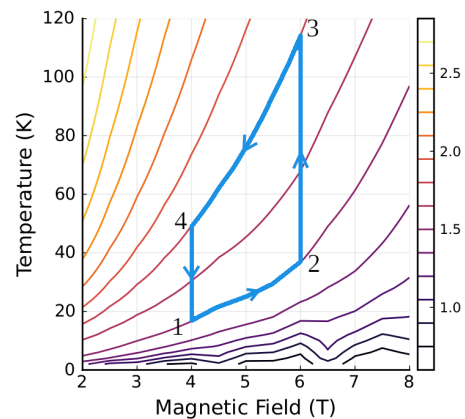


FIG. 6. Isentropic lines on the temperature–magnetic field plane for twisted bilayer graphene at magic angle. A possible Otto cycle with general adiabatic conditions is traced out in blue.

heat engine [42] it is implemented by a suitable sequence of rf pulses. Recently, there have been experiments measuring the magnetic entropy of magic-angle graphene at low temperatures, which has led to the discovery of an electronic phase transition at zero magnetic field [26, 27]. These experiments demonstrate the possibility of precisely controlling the thermodynamic state of MATBG in a laboratory that could implement isochores of the Otto cycle proposed in this paper. In particular, Fig. 6 shows how the temperature and magnetic field should be simultaneously changed to implement the cycle.

We note that a Carnot cycle with MATBG can be designed analogously by using two adiabatic and two isothermal strokes. While the efficiency of a Carnot cycle is fixed at  $\eta_C = 1 - T_C/T_H$  independent of expansion ratio [2, 17], it will be interesting to see what impact magic angle twists have on work output. After looking at a highly efficient quantum heat engine based on MATBG, a natural question to ask next is if it might be possible to use MATBG to design a nanoscale refrigerator with a high coefficient of performance. Both these possibilities will be explored in a future work [43].

## ACKNOWLEDGMENTS

This work was supported by the grants: 1. Josephson junctions with strained Dirac materials and their application

in quantum information processing, Science & Engineering Research Board (SERB) Grant No. CRG/2019/006258, and 2. Nash equilibrium versus Pareto optimality in N-Player games, Science & Engineering Research Board (SERB) MATRICS Grant No. MTR/2018/000070.

- [1] F. Binder, L. Correa, C. Gogolin, J. Anders, and G. Adesso, eds., *Thermodynamics in the Quantum Regime* (Springer Cham., 2019).
- [2] H. T. Quan, Y.-x. Liu, C. P. Sun, and F. Nori, Quantum thermodynamic cycles and quantum heat engines, *Phys. Rev. E* **76**, 031105 (2007).
- [3] H. T. Quan, Quantum thermodynamic cycles and quantum heat engines. ii., *Phys. Rev. E* **79**, 041129 (2009).
- [4] Y. Rezek and R. Kosloff, Irreversible performance of a quantum harmonic heat engine, *New Journal of Physics* **8**, 83 (2006).
- [5] H. T. Quan, P. Zhang, and C. P. Sun, Quantum heat engine with multilevel quantum systems, *Phys. Rev. E* **72**, 056110 (2005).
- [6] R. Uzdin and R. Kosloff, Universal features in the efficiency at maximal work of hot quantum Otto engines, *EPL (Europhysics Letters)* **108**, 40001 (2014).
- [7] S. Vinjanampathy and J. Anders, Quantum thermodynamics, *Contemporary Physics* **57**, 545 (2016).
- [8] M. O. Scully, Extracting work from a single thermal bath via quantum negentropy, *Phys. Rev. Lett.* **87**, 220601 (2001).
- [9] J. Roßnagel, O. Abah, F. Schmidt-Kaler, K. Singer, and E. Lutz, Nanoscale heat engine beyond the carnot limit, *Phys. Rev. Lett.* **112**, 030602 (2014).
- [10] M. O. Scully, K. R. Chapin, K. E. Dorfman, M. B. Kim, and A. Svidzinsky, Quantum heat engine power can be increased by noise-induced coherence, *Proceedings of the National Academy of Sciences* **108**, 15097 (2011), <https://www.pnas.org/content/108/37/15097.full.pdf>.
- [11] M. O. Scully, M. S. Zubairy, G. S. Agarwal, and H. Walther, Extracting work from a single heat bath via vanishing quantum coherence, *Science* **299**, 862 (2003), <https://science.sciencemag.org/content/299/5608/862.full.pdf>.
- [12] K. E. Dorfman, D. V. Voronine, S. Mukamel, and M. O. Scully, Photosynthetic reaction center as a quantum heat engine, *Proceedings of the National Academy of Sciences* **110**, 2746 (2013), <https://www.pnas.org/content/110/8/2746.full.pdf>.
- [13] R. Alicki, D. Gelbwaser-Klimovsky, and A. Jenkins, A thermodynamic cycle for the solar cell, *Annals of Physics* **378**, 71 (2017).
- [14] T. D. Kieu, The second law, Maxwell's demon, and work derivable from quantum heat engines, *Phys. Rev. Lett.* **93**, 140403 (2004).
- [15] R. Alicki, M. Horodecki, P. Horodecki, and R. Horodecki, Thermodynamics of quantum information systems — hamiltonian description, *Open Systems & Information Dynamics* **11**, 205 (2004), <https://doi.org/10.1023/B:OPSY.0000047566.72717.71>.
- [16] S. Toyabe, T. Sagawa, M. Ueda, E. Muneyuki, and M. Sano, Experimental demonstration of information-to-energy conversion and validation of the generalized jarzynski equality, *Nature Physics* **6**, 988 (2010).
- [17] E. Muñoz and F. J. Peña, Magnetically driven quantum heat engine, *Phys. Rev. E* **89**, 052107 (2014).
- [18] F. J. Peña, O. Negrete, G. Alvarado Barrios, D. Zambrano, A. González, A. S. Nunez, P. A. Orellana, and P. Vargas, Magnetic Otto engine for an electron in a quantum dot: Classical and quantum approach, *Entropy* **21**, 10.3390/e21050512 (2019).
- [19] F. J. Peña, D. Zambrano, O. Negrete, G. De Chiara, P. A. Orellana, and P. Vargas, Quasistatic and quantum-adiabatic Otto engine for a two-dimensional material: The case of a graphene quantum dot, *Phys. Rev. E* **101**, 012116 (2020).
- [20] F. Peña, O. Negrete, N. Cortés, and P. Vargas, Otto engine: Classical and quantum approach, *Entropy (Basel)* **22**, 10.3390/e22070755.
- [21] F. J. Peña and E. Muñoz, Magnetostrain-driven quantum engine on a graphene flake, *Phys. Rev. E* **91**, 052152 (2015).
- [22] R. Bistritzer and A. H. MacDonald, Moiré bands in twisted double-layer graphene, *Proceedings of the National Academy of Sciences* **108**, 12233 (2011), <https://www.pnas.org/content/108/30/12233.full.pdf>.
- [23] J. M. B. Lopes dos Santos, N. M. R. Peres, and A. H. Castro Neto, Continuum model of the twisted graphene bilayer, *Phys. Rev. B* **86**, 155449 (2012).
- [24] Y. Cao, V. Fatemi, A. Demir, S. Fang, S. L. Tomarken, J. Y. Luo, J. D. Sanchez-Yamagishi, K. Watanabe, E. Kaxiras, R. C. Ashoori, and P. Jarillo-Herrero, Correlated insulator behaviour at half-filling in magic-angle graphene superlattices, *Nature* **556**, 80 (2018).
- [25] Y. Cao, V. Fatemi, S. Fang, K. Watanabe, T. Taniguchi, E. Kaxiras, and P. Jarillo-Herrero, Unconventional superconductivity in magic-angle graphene superlattices, *Nature* **556**, 43 (2018).
- [26] Y. Saito, F. Yang, J. Ge, X. Liu, T. Taniguchi, K. Watanabe, J. I. A. Li, E. Berg, and A. F. Young, Isospin Pomeranchuk effect in twisted bilayer graphene, *Nature* **592**, 220 (2021).
- [27] A. Rozen, J. M. Park, U. Zondiner, Y. Cao, D. Rodan-Legrain, T. Taniguchi, K. Watanabe, Y. Oreg, A. Stern, E. Berg, P. Jarillo-Herrero, and S. Ilani, Entropic evidence for a Pomeranchuk effect in magic-angle graphene, *Nature* **592**, 214 (2021).
- [28] O. Abah, J. Roßnagel, G. Jacob, S. Deffner, F. Schmidt-Kaler, K. Singer, and E. Lutz, Single-ion heat engine at maximum power, *Phys. Rev. Lett.* **109**, 203006 (2012).
- [29] J. M. B. Lopes dos Santos, N. M. R. Peres, and A. H. Castro Neto, Graphene bilayer with a twist: Electronic structure, *Phys. Rev. Lett.* **99**, 256802 (2007).
- [30] R. Bistritzer and A. H. MacDonald, Moiré butterflies in twisted bilayer graphene, *Phys. Rev. B* **84**, 035440 (2011).
- [31] J. Python, *Quantum oscillations in twisted bilayer graphene*, Master's thesis, Utrecht University (2019).
- [32] M. O. Goerbig, Electronic properties of graphene in a strong magnetic field, *Rev. Mod. Phys.* **83**, 1193 (2011).
- [33] E. McCann and M. Koshino, The electronic properties of bilayer graphene, *Reports on Progress in Physics* **76**, 056503 (2013).
- [34] E. McCann and V. I. Fal'ko, Landau-level degeneracy and quantum Hall effect in a graphite bilayer, *Phys. Rev. Lett.* **96**, 086805 (2006).
- [35] R. de Gail, M. O. Goerbig, F. Guinea, G. Montambaux, and A. H. Castro Neto, Topologically protected zero modes in twisted bilayer graphene, *Phys. Rev. B* **84**, 045436 (2011).
- [36] P. Moon and M. Koshino, Energy spectrum and quantum Hall effect in twisted bilayer graphene, *Phys. Rev. B* **85**, 195458

(2012).

- [37] Y.-H. Zhang, H. C. Po, and T. Senthil, Landau level degeneracy in twisted bilayer graphene: Role of symmetry breaking, *Phys. Rev. B* **100**, 125104 (2019).
- [38] E. Suárez Morell, J. D. Correa, P. Vargas, M. Pacheco, and Z. Barticevic, Flat bands in slightly twisted bilayer graphene: Tight-binding calculations, *Phys. Rev. B* **82**, 121407 (R) (2010).
- [39] Julia code used to determine (a) Landau levels numerically for MATBG is available at <https://github.com/11DE784A/bilayer/blob/9640d61330b81cb22ab0fe65bdcb6d73da27475/Spectra.jl> (b) efficiencies and work done for quantum Otto engine with TBG is available at <https://github.com/11DE784A/bilayer/blob/9640d61330b81cb22ab0fe65bdcb6d73da27475/Otto.jl>.
- [40]  $\gamma = C_p/C_V$  is the ratio of specific heats at constant pressure and constant volume.
- [41] W. Niedenzu, D. Gelbwaser-Klimovsky, and G. Kurizki, Performance limits of multilevel and multipartite quantum heat machines, *Phys. Rev. E* **92**, 042123 (2015).
- [42] J. P. S. Peterson, T. B. Batalhão, M. Herrera, A. M. Souza, R. S. Sarthour, I. S. Oliveira, and R. M. Serra, Experimental characterization of a spin quantum heat engine, *Phys. Rev. Lett.* **123**, 240601 (2019).
- [43] A. Singh and C. Benjamin, Manuscript under preparation.

### Appendix A: Equivalence of conservation of thermal populations and the adiabatic condition

For monolayer graphene we have

$$E_n^{\text{mono}}(B) = \frac{\hbar v_F}{l_B} \sqrt{2n}, \quad (\text{A1})$$

where  $l_B = \sqrt{\hbar/eB}$ . If the magnetic field is changed from  $B_1$  to  $B_2$ , we get

$$\begin{aligned} E_n^{\text{mono}}(B_2) &= \frac{\hbar v_F}{l_{B_2}} \sqrt{2n} \\ &= \sqrt{\frac{B_2}{B_1}} \frac{\hbar v_F}{l_{B_1}} \sqrt{2n} = \sqrt{\frac{B_2}{B_1}} E_n^{\text{mono}}(B_1). \end{aligned} \quad (\text{A2})$$

Similarly, as for bilayer graphene the Landau levels are  $E_n^{\text{bi}} = \hbar\omega_B \sqrt{n(n-1)}$ , with  $\omega_B = eB/m_{\text{eff}}$ , we get

$$\begin{aligned} E_n^{\text{bi}}(B_2) &= \hbar\omega_{B_2} \sqrt{n(n-1)} \\ &= \frac{B_2}{B_1} \omega_{B_1} \sqrt{n(n-1)} = \frac{B_2}{B_1} E_n^{\text{bi}}(B_1). \end{aligned} \quad (\text{A3})$$

In both these cases, we have  $E_n(B_2) = \zeta E_n(B_1)$ , where  $\zeta$  is a constant independent of  $n$ , but which depends on the ratio  $B_2/B_1$ .

First we note that the conservation of thermal populations  $P_n(B_1, T_1) = P_n(B_2, T_2)$  implies  $S(B_1, T_1) = S(B_2, T_2)$  because  $S(B, T) = -\sum_n P_n(B, T) \ln P_n(B, T)$ . The converse can be proven if we consider the special case when energy levels change in the same ratio, i.e.,  $E_n(B) \rightarrow \zeta E_n(B)$ . In thermal

equilibrium, the occupation probability of each Landau level  $E_n$  is given by the Boltzmann distribution

$$P_n(B, T) = \frac{e^{-\beta E_n(B)}}{Z(B, T)}; \quad Z(B, T) = \sum_{n=0}^{\infty} e^{-\beta E_n(B)}, \quad (\text{A4})$$

and we have

$$\frac{P_n(B_1, T_1)}{P_m(B_1, T_1)} = \frac{e^{-\beta_1 E_n(B_1)}}{e^{-\beta_1 E_m(B_1)}} \quad (\text{A5})$$

and

$$\frac{P_n(B_2, T_2)}{P_m(B_2, T_2)} = \frac{e^{-\beta_2 E_n(B_2)}}{e^{-\beta_2 E_m(B_2)}} = \frac{e^{-\zeta \beta_2 E_n(B_1)}}{e^{-\zeta \beta_2 E_m(B_1)}} \quad (\text{A6})$$

If the temperature at the end of the cycle is chosen to be  $T_2 = \zeta T_1$  so that  $\beta_1 = \zeta \beta_2$ , then for every  $m$  and  $n$  we have

$$\begin{aligned} \frac{P_n(B_1, T_1)}{P_m(B_1, T_1)} &= \frac{P_n(B_2, T_2)}{P_m(B_2, T_2)} \\ \implies \frac{P_n(B_1, T_1)}{P_n(B_2, T_2)} &= \frac{P_m(B_1, T_1)}{P_m(B_2, T_2)} = \lambda \quad (\text{say}). \end{aligned} \quad (\text{A7})$$

Now, we if impose the adiabatic condition  $S(B_1, T_1) = S(B_2, T_2)$ , we get

$$\begin{aligned} &\sum_n P_n(B_2, T_2) \ln P_n(B_2, T_2) \\ &= \sum_n P_n(B_1, T_1) \ln P_n(B_1, T_1) \\ &= \sum_n \lambda P_n(B_2, T_2) [\ln \lambda + \ln P_n(B_2, T_2)] \\ &= \lambda \sum_n P_n(B_2, T_2) \ln P_n(B_2, T_2) + \lambda \ln \lambda, \end{aligned} \quad (\text{A8})$$

which gives the following equation for  $\lambda$

$$(\lambda - 1)S(B_2, T_2) = \lambda \ln \lambda. \quad (\text{A9})$$

Since (A7) holds independent of particular values of temperature and magnetic field, the solution to  $\lambda$  in the above equation must not depend on  $S(B_2, T_2)$ . In such a scenario, the only solution is  $\lambda = 1$ , and from (A7) we have

$$P_n(B_1, T_1) = P_n(B_2, T_2) \quad (\text{A10})$$

in an adiabatic process.

### Appendix B: Quantum Otto engine cycle with strict adiabatic condition

Although the main text focuses on the heat engine cycle with general adiabatic strokes, a stricter version of the cycle can also be described very similarly herein. The two general adiabatic strokes are swapped out for stricter adiabatic strokes. We require the stronger condition:  $p_n(i) = p_n(f)$ , and the cycle is identical to Fig. 3 in all other respects.



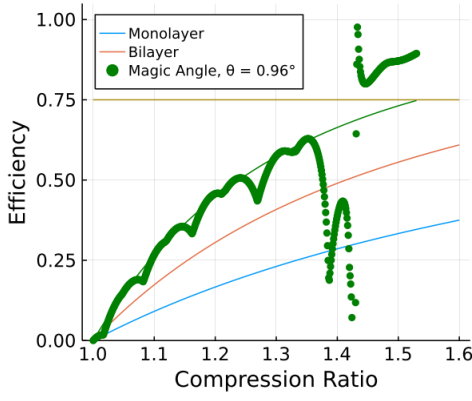


FIG. 7. Efficiencies as a function of the compression ratio for Otto cycles operating between  $T_C = 10$  K and  $T_H = 40$  K, and  $B_1 = 3.0$  T with strict adiabatic conditions. There is a divergence at compression ratio = 1.43 as Work done changes sign, see Fig. 8. The green solid line is the least squares fit for case of MATBG. Obviously, efficiency is not defined for values of compression ratio beyond 1.43 for MATBG.

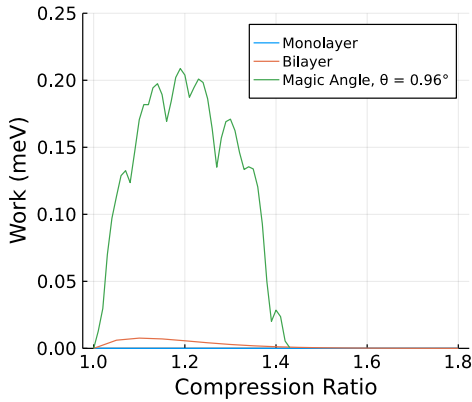


FIG. 8. Work outputs as a function of the compression ratio for Otto cycles operating between  $T_C = 10$  K and  $T_H = 40$  K, and  $B_1 = 3.0$  T with strict adiabatic conditions.

We start with the graphene sample at temperature  $T_C$  and Landau radius  $l_{B_1}$ . Strict adiabatic compression implies, magnetic field is changed very slowly  $l_{B_1} \rightarrow l_{B_2}$ , so that  $dp_n = 0$  and the quantum condition

$$p_n(T_C, B_1) = p_n(2) \quad (B1)$$

is satisfied. At the end of this stroke, the occupation probabilities will not satisfy a Boltzmann distribution unless the energy levels change in the same ratio, and the working substance will not, in general, be in a state with well defined temperature.

The second stroke is the hot isochore; working substance is coupled with the heat reservoir at temperature  $T_H$ , and the it absorbs heat. In complete analogy to the classical case, heat

exchanged is given by

$$Q_{2 \rightarrow 3} = \sum_{n=0}^{\infty} E_n(B_2) [p_n(T_H, B_2) - p_n(2)]. \quad (B2)$$

TABLE II. A comparison of efficiencies and work outputs for Otto cycle operating with strict adiabatic conditions.

Working Substance	Efficiency	Work (meV)
Monolayer Graphene	$1 - r_C^{-1.00}$	0.000169
Bilayer Graphene	$1 - r_C^{-2.00}$	0.00758
Magic Angle Twisted Bilayer ( $\theta^* = 0.96^\circ$ )	$1 - r_C^{-3.24}$	0.204

Next, in the adiabatic expansion  $l_{B_2} \rightarrow l_{B_1}$ , the magnetic field is changed slowly so that the strict adiabatic condition

$$p_n(T_H, B_2) = p_n(4) \quad (B3)$$

is satisfied. As before, the working substance does not have a well defined temperature at the end of this stroke. Finally, we have the cold isochore. The working substance is coupled with the reservoir at temperature  $T_H$  and the system returns to its initial state. As before, the heat exchanged is given by

$$Q_{4 \rightarrow 1} = \sum_{n=0}^{\infty} E_n(B_1) [p_n(T_C, B_1) - p_n(4)], \quad (B4)$$

and we use the quantum first law of thermodynamics (12) to write the work output

$$|W_0| = |Q_{2 \rightarrow 3}| - |Q_{4 \rightarrow 1}|, \quad (B5)$$

and efficiency

$$\eta_0 = 1 - \left| \frac{\sum_n E_n(B_1) [p_n(T_C, B_1) - p_n(4)]}{\sum_n E_n(B_2) [p_n(T_H, B_2) - p_n(2)]} \right|. \quad (B6)$$

We use the above relations to compute efficiencies (Fig. 7) and work output (Fig. 8) in the Otto cycle with strict adiabatic conditions. To achieve optimal performance in the quantum case, we take  $T_C = 10$  K,  $T_H = 40$  K and  $B_1 = 3.0$  T. As the nature of adiabatic strokes differs between general and strict cycles, it is not surprising that optimal performance is achieved for different parameter values in both cases.

As in the general case, we do a curve fitting for  $\alpha$  in  $\eta = 1 - r_C^{-\alpha}$  and find that  $\alpha = 3.24$  for the magic angle. Results are summarized in Table II. Although as compared to the general case, the efficiency in case MATBG has decreased a bit but is still much more efficient than mono or bi-layer. Work done in a strict QOE cycle has increased much more than the general cycle. Work done for the strict QOE cycle is almost 30 times that seen in bilayer case, while that in general QOE cycle is 7 times that in bilayer case.